Nanoscale

RSC Publishing

PAPER

Nanorod–nanosheet hierarchically structured ZnO crystals on zinc foil as flexible photoanodes for dye-sensitized solar cells

Cite this: *Nanoscale*, 2013, **5**, 1894

Rui Gao,[ab] Jianjun Tian,[a] Zhiqiang Liang,[a] Qifeng Zhang,[a] Liduo Wang*[b] and Guozhong Cao*[a]

Received 12th November 2012
Accepted 22nd December 2012

DOI: 10.1039/c2nr33599a

www.rsc.org/nanoscale

In this paper, ZnO nanorod–nanosheet hierarchical structures were fabricated using a facile method on zinc foil and used as flexible photoanodes in dye-sensitized solar cells (DSCs). Compared to nanorods (NRs) obtained by the dissolution–precipitation method, the nanorod–nanosheet (NR–NS) hierarchical structures obtained by a second-step homogeneous precipitation improved the performance of DSCs by increasing photocurrent density significantly. As a result, the power conversion efficiency of the devices based on such a NR–NS hierarchical structure reached up to 2.4% under 100 mW cm^{-2} illumination condition. This represents an enhancement by 108% as compared to DSCs based on NR assembled nanoflowers, for which the efficiency was 1.1%. The enhancement of the photocurrent was due mainly to the much larger specific surface area and resulting dye-loading amount. The electron transport properties in this structure were also investigated by means of electrochemical impedance spectroscopy (EIS). Furthermore, the formation mechanism of the NR–NS hierarchical structures are discussed.

1 Introduction

Dye-sensitized solar cells (DSCs) are considered as an alternative to conventional silicon based solar cells due to their lower cost and easier fabrication, ever since a photoanode made of porous titania was reported first in 1991.[1] Much attention had been focused on efficiency enhancement[2–8] and stability improvement[9–15] of DSCs. The power conversion efficiency of DSCs based on TiO_2 photoanode has now reached over 13%.[16] The photoanode is a vital factor to improve the performance of DSCs, thus much study had been conducted on materials for photoanodes of DSCs. Besides TiO_2, other oxide semiconductors with wide bandgaps have also been studied, including ZnO, SnO_2, Nb_2O_5 and so on.[17–23] Among these materials, ZnO with different structures has been intensively investigated owing to its easier synthesis process and higher electron mobility compared to TiO_2. Because of the significant electron mobility, ZnO with ordered structures, especially one-dimensional nanostructures were considered as ideal structures for photoanodes. Thus ZnO nanotubes, nanorods and nanowires have been synthesized and expected to obtain high conversion efficiency of DSCs. Flexible DSCs is a new research field showing potential application in mobile electronic products. Much attention has been focused on this promising area for its versatility and low cost. Up to now, two kinds of flexible substrates have been used, metal sheets[24] and polymer substrates.[25] Metal sheets have low resistance and are easier to make flexible DSCs devices.[24,26] However, DSC devices based on metal sheets showed much lower conversion efficiency than those based on FTO glass, due to light absorption of electrolyte and other reasons such as illumination being from the direction of the counter electrode.[27,28] As a result, much study has been done to enhance the conversion efficiency of such DSCs. In this work, an *in situ* precipitation method[29] was used to synthesize nanoflowers composed of nanorods (NR) on zinc foil which could be used as a flexible photoanode for DSCs. Compared with other routes such as electrochemical deposition, physical/chemical vapor deposition or hydrothermal methods, this method features simpler operation and lower cost, and is more suited for industrial production.

However, DSCs based on one-dimensional (1-D) structures have not reached high conversion efficiency as expected, though showing fast electron transportation. This may be because the 1-D structures have a much smaller surface area for dye adsorption compared with nanoparticles. Constructing hierarchical morphologies based on 1-D structures and nanoparticles turns out to be an effective way to improve the surface area significantly.[30–34] Cao *et al.* made nanoparticles and nanowire array hybrid photoanodes by spin-coating a colloidal dispersion of ZnO nanoparticles on top of ZnO nanowire arrays.[33] Using a two-step hydrothermal process, Kuang *et al.* synthesized hierarchical TiO_2 for a flexible photoanode of DSCs. The power

[a]*Department of Materials Science and Engineering, University of Washington, Seattle, WA 98195, USA. E-mail: gzcao@u.washington.edu*

[b]*Key Lab of Organic Optoelectronics & Molecular Engineering of Ministry of Education, Department of Chemistry, Tsinghua University, Beijing 100084, China. E-mail: chldwang@mail.tsinghua.edu.cn*

conversion efficiency of DSCs based on the hierarchical structure (4.51%) showed a significant enhancement compared to that of the nanorod photoanode (3.12%).[35] However, the hydrothermal method is not simple and requires substantial heating. To avoid such disadvantages, a facile method through homogeneous precipitation at much lower temperature than that of the hydrothermal method was developed here to fabricate a nanorod–nanosheet (NR–NS) hierarchical structure. Besides, this method is much easier to process. As a result, the conversion efficiency showed a significant enhancement using such an optimized hierarchical structure as photoanode of DSCs. Furthermore, the electron transport properties and assembling mechanism of such structured photoanodes are also discussed.

2 Experimental

2.1 Synthesizing ZnO nanoflowers and hierarchical structure on the zinc foil

The alkali zincate solution was prepared by adding dropwise 10 mL 0.5 M aqueous solution of $Zn(NO_3)_2 \cdot 6H_2O$ into 10 mL 4.0 M aqueous solution of KOH under stirring. The growth of ZnO nanorods assembled nanoflowers were achieved by suspending a clean zinc foil upside down in 20 mL zincate solution and sealing the system in a beaker. After reaction at 25 °C for 8 h, the zinc foil was taken out and rinsed with de-ionized water.

The second process was transferring the zinc foil obtained in the previous process into a 100 mL glass bottle containing 0.01 M $Zn(NO_3)_2$, 0.01 M hexamethylene tetramine (HMT) and 0.001 M sodium citrate aqueous solution, and heating at different temperature for 6 h.

2.2 Assembly of the DSCs

The ZnO photoanode was sintered at 300 °C, then sensitized in 0.3 mM N719 absolute ethanol solution for 60 min at 50 °C,[36] followed by cleaning with absolute ethanol. The electrolyte is a liquid admixture containing 0.5 M tetrabutylammonium iodide, 0.1 M lithium iodide, 0.1 M iodine and 0.5 M 4-*tert*-butylpyridine in acetonitrile. A transparent platinized conductive glass was used as the counter electrode. When assembling the DSCs, the electrolyte was sandwiched by a sensitized ZnO on the zinc foil and a counter electrode with two clips. The illumination was from the direction of the counter electrode.

2.3 Characterization

The morphologies of the different ZnO films were characterized by scanning electron microscopy (SEM, JEOL JSM-7000). X-Ray diffraction (Philips PW1830 Diffractometer) and JADE software (MDI JADE 7 Materials Data XRD Pattern Processing, Identification, and Quantification) were used to verify the phase and crystal structure of the ZnO films. The photovoltaic behavior was characterized when the cell devices were irradiated by simulated AM 1.5 sunlight with an output power of 100 mW cm^{-2}. An Ultraviolet Solar Simulator (model 16S, Solar Light Co., Philadelphia, PA) with a 200 W Xenon Lamp Power Supply (Model XPS 200, Solar Light Co., Philadelphia, PA) was used as the light source, and a Semiconductor Parameter Analyzer (4155A, Hewlett–Packard, Japan) was used to measure the current and voltage curves. Electrochemical impedance spectroscopy (EIS) was carried out through the Solartron 1287A coupling with the Solartron 1260 FRA/impedance analyzer to investigate electronic and ionic processes in DSCs.

3 Results and discussion

As shown in Fig. 1a and b, using a dissolution–precipitation method, nanorod assembled nanoflowers were obtained on the zinc foil surface.[29] Fig. 1c shows the cross section SEM image of ZnO nanoflowers on the zinc foil from which it could be seen that the thickness of ZnO was about 40 μm (41 μm). Owing to the much higher electron mobility of ZnO compared to TiO_2 it can be fabricated as a much thicker layer than that of TiO_2.[37] The ordered porous structure should also facilitate the filling of electrolyte into the sensitized films. Fig. 1d shows the XRD spectra of ZnO nanorods assembled nanoflowers on the zinc foil. The XRD peaks can be very well indexed to ZnO (Joint Committee on Powder Diffraction Standards—JCPDS card number 36-1451).

However, one key challenge of using such 1-D nanostructures in DSCs is that in comparison with porous films, the 1-D nanostructure typically has a low internal surface area, resulting in insufficient dye adsorption and therefore low light-harvesting efficiency. Constructing hierarchical morphologies based on 1-D structures and nanoparticles turns out to be an effective way to improve the surface area significantly. Thus NR–NS hierarchically structures are fabricated using a second-step homogeneous precipitation method at different temperatures to enhance the dye-loading and conversion efficiency of DSCs based on flexible photoanodes.

As shown in Fig. 2c and d, ultra-thin nanosheets formed and attached on the nanorods to form a NR–NS hierarchical structure at 60 °C. It was clearly observed that the smooth surfaces of the NRs shown in Fig. 2a and b were surrounded by NS. The

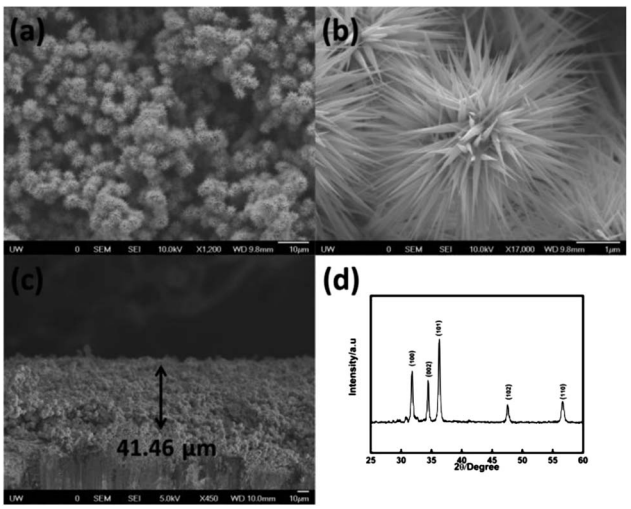

Fig. 1 (a), (b), (c) SEM images and (d) XRD spectrum of ZnO nanorod assembled nanoflowers on zinc foil obtained through the dissolution–precipitation method.

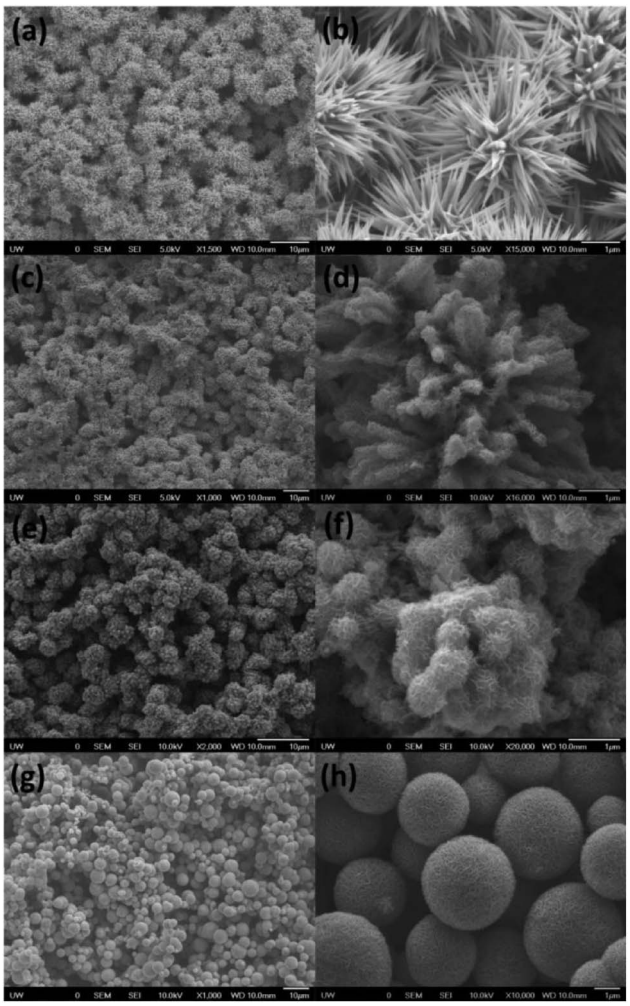

Fig. 2 SEM images of (a), (b) ZnO NR assembled nanoflowers, and of NR–NS hierarchical structures through a second precipitation process using $Zn(NO_3)_2$, HMT and sodium citrate at (c), (d) 60 °C; (e), (f) 70 °C and (g), (h) 80 °C.

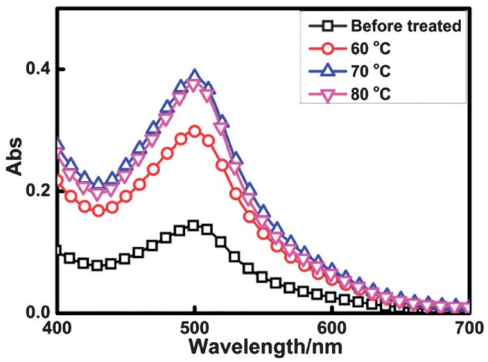

Fig. 3 UV-Vis absorbance spectra of solutions containing dyes desorbed from the sensitized photoanodes composed of NR assembled nanoflowers and NR–NS hierarchical structures formed at different temperatures.

diameter of the NRs increased obviously compared with that shown in Fig. 2b. As the temperature was increased to 70 °C, the NS further assemble on the NRs, then formed nanospheres (NSp) with diameter of 500–700 nm, thus the nanoflowers turned to a cauliflower structure, which were shown in Fig. 2e and f. As the temperature was further raised to 80 °C, it was found that much bigger sized microspheres than that formed at 70 °C was assembled by NS, which was consistent with earlier reports by Lu *et al.*[38] As shown in Fig. 2g and h, the diameter of the NSp were 3–4 μm, which was almost same as the size of the nanoflowers shown in Fig. 1. Furthermore, at a higher temperature of 80 °C, nucleation occurred very rapidly in the solution and attachment together led to the microspheres. Then the microspheres precipitated and located on the top of nanoflowers before attaching on the nanorods. Thus the NSp was partly assembled from nanoflowers and others from direct precipitation. Such three different morphologies could lead to much larger surface area and more dye-loading amount. Fig. 3 shows the UV-Vis absorption spectra of solutions containing dyes desorbed from the sensitized ZnO films composed of nanoflowers and NR–NS hierarchical structure formed at different temperature. It could be observed that the NR–NS structures all showed much more dye-loading amount than NR assembled nanoflowers. As shown in Fig. 3, the 70 °C treated sample showed the largest dye-loading. Detailed data is listed in Table 1. The dye-loading of NR assembled nanoflowers was 135 nmol cm^{-2}, and increased to 282 nmol cm^{-2} when the NR–NS hierarchical structure at 60 °C was formed, as the temperature was increased to 70 °C, the dye-loading further increased to 365 nmol cm^{-2}, which showed 170% enhancement. However, the dye-loading decreased a little to 355 nmol cm^{-2} as the temperature was further increased to 80 °C. This could be due to the surface area decreasing as the cauliflower structure turned to much bigger spheres as shown in Fig. 2g and h. Generally, a large dye absorption amount could make sure that the introduced photons are fully absorbed, resulting in a larger photocurrent and consequently improving the overall conversion efficiency. The ZnO films with different structures were used as photoanodes of back-illuminated DSCs. The structure of such devices are shown in Scheme 1. The illumination was from the counter electrode direction.

As shown in Fig. 4, enhanced dye-loading caused an increase of photocurrent. The parameters of photovoltaic performance are listed in Table 2. Compared to untreated NR assembled nanoflowers, the short circuit current density (J_{sc}) of devices based on the NR–NS hierarchical structure obtained at different temperature all increased. It was enhanced from 3.81 mA cm^{-2} to 10.31, 11.40 and 10.63 mA cm^{-2} at 60, 70 and 80 °C, respectively. The largest J_{sc} was obtained at 70 °C with nearly 200% enhancement compared to the NR structure, which also

Table 1 Dye-loading amounts of untreated NR and NR–NS hierarchical structured ZnO formed at different treatment temperatures *T*

T/°C	Dye-loading/nmol cm^{-2}
Untreated	135
60	282
70	365
80	355

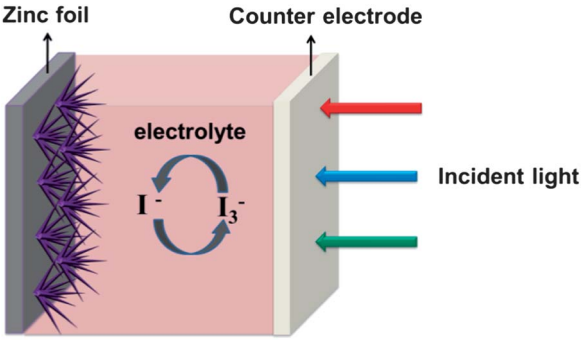

Scheme 1 Structure of back-illuminated DSCs device based on flexible photoanode of zinc foil.

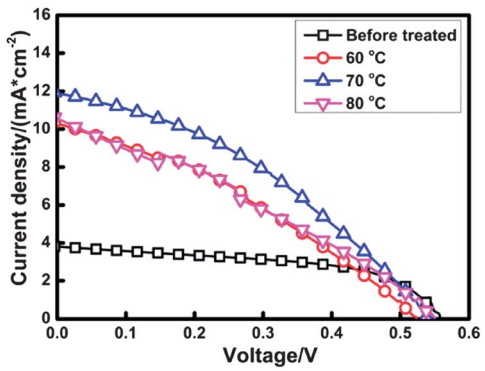

Fig. 4 *J–V* curves of DSCs devices based on ZnO NR assembled nanoflowers without treatment and NR–NS hierarchical structures formed by a secondary precipitation process at different temperatures.

Table 2 Parameters of photovoltaic performance of DSCs devices based on ZnO nanoflowers and hierarchical structures formed at different temperatures *T*

T/°C	J_{sc}/mA cm^2	V_{oc}/V	FF	η (%)
Untreated	3.81	0.56	0.53	1.14
60	10.31	0.52	0.33	1.79
70	11.94	0.54	0.37	2.38
80	10.63	0.55	0.30	1.78

accorded with the results of dye-loading. However, when the NR–NS hierarchical structure was assembled, the open circuit voltage (V_{oc}) decreased a little and the fill factor also decreased from 0.53 to 0.33, 0.37 and 0.30 at 60, 70 and 80 °C, respectively. As the 1-D structure is beneficial for electron transport in the ZnO film, the electron transport could be slowed when the 1-D structure was changed to a 3-D hierarchical structure. As a result, the conversion efficiency of devices based on a hierarchical structure obtained at 70 °C was 2.38% at AM 1.5, 100 mW cm^{-2} illumination, with a relative enhancement of 108% compared to that based on untreated nanoflowers (1.14%). However, the decreased V_{oc} and fill factor (FF) limited the improvement of the performance of DSCs based on the NR–NS hierarchically structure. To further investigate the effects of charge transport and recombination on V_{oc} and FF in such NR–NS hierarchically structured ZnO film, electrochemical impedance spectroscopy (EIS) of devices based on different structured ZnO were tested. EIS is a well-established technique in characterizing DSCs because it shows all kinetic processes of DSCs such as electron transport in the photoanode, recombination property at the oxide–electrolyte interface, charge transfer at the counter electrode–electrolyte interface, and electron diffusion in an electrolyte.[39–42] Electrons were injected into the ZnO film from zinc foil substrate when a bias voltage was applied in dark condition. Then the ZnO film became charged by transport of the injected electrons. Meanwhile, some of the injected electrons in the conduction band of ZnO recombined with I^-/I_3^- redox in the electrolyte. These processes were denoted as semicircles at different frequency ranges in a Nyquist plot. Charge transfer at the zinc–ZnO interface was at >10^5 Hz. Charge transport in the ZnO film and charge transfer at the counter electrode–electrolyte interface was in the range of 10^5 to 10^3 Hz, charge transfer at the ZnO–electrolyte interface was around 10^1 Hz, and ion diffusion in the electrolyte was below 1 Hz.[40,43,44]

In this paper, the EIS was tested under open circuit in dark condition. As shown in Fig. 5a, the Nyquist plot simply displayed a charge transfer resistance at the counter electrode–electrolyte interface (R_c) and the ZnO network–electrolyte interface (R_{ct}). The smaller semicircle represented R_c and the larger one represented R_{ct}, respectively. The results shown in Fig. 5a indicated that R_{ct} of device based on ZnO NR–NS structure (70 °C) was larger than that based on NRs. Thus the

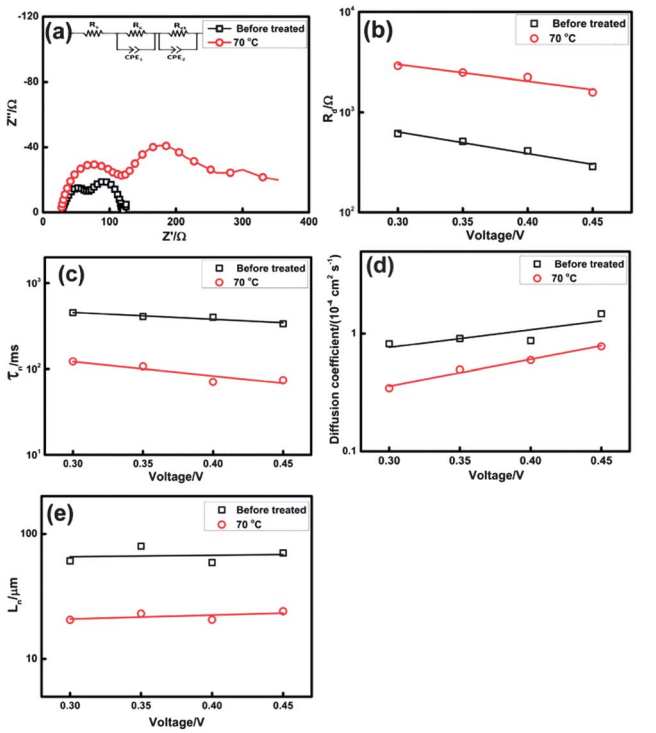

Fig. 5 (a) Nyquist plot tested at a bias voltage of −0.7 V, (b) diffusion resistance at low bias voltage, (c) electron lifetime, (d) diffusion coefficient and (e) electron diffusion length of devices based on ZnO nanoflowers and hierarchical structure formed at 70 °C; the EIS was tested in dark condition.

charge transfer from the conductive band of ZnO to the redox in the electrolyte, which was the charge recombination, was more difficult in the NR–NS structure. A diffusion resistance (R_d) representing the effectiveness of charge transport occurring by diffusion along the ZnO network could not be distinguished from R_c and R_{ct} at this condition because R_d was overlapped with R_c and R_{ct} at the position where the transition from R_c to R_{ct} occurs. Yet, with a decrease of the bias voltage from the open circuit condition, a diffusion resistance is noted as Warburg-like diffusion starts to appear with an increase in R_{ct}.[45] As shown in Fig. 5b, the value of R_d at the relative lower bias voltage decreased obviously from the ZnO NRs to the NR–NS hierarchical structure. As the 1-D structure was beneficial for the electron diffusion, it decreased as it changed to a hierarchical structure. Separating R_d from R_{ct} is useful because charge transport properties such as electron lifetime (τ_n), electron diffusion coefficient (D_n) and diffusion length (L_n) could be calculated by using R_{ct}, R_d, and the corresponding chemical capacitance (C_μ) as follows:[39]

$$\tau_n = R_{ct}C_\mu \quad (1)$$

$$D_n = L^2/R_dC_\mu \quad (2)$$

$$L_n = \sqrt{D_n\tau_n} \quad (3)$$

The charge transport properties in DSCs are widely characterized in terms of electron lifetime, τ_n, and electron diffusion coefficient, D_n. A variety of methods have been applied to measure them, including intensity modulated photovoltage spectroscopy (IMVS) and V_{oc} decay method for τ_n and intensity modulated photocurrent spectroscopy (IMPS) for the diffusion coefficient (D_n).[46–48] Electrochemical impedance spectroscopy (EIS) is also widely used for the measurement of τ_n and D_n, and the results of EIS were consistent with other methods.[49,50]

Commonly, weaker charge recombination means a higher V_{oc}. However, as shown in Fig. 4, the V_{oc} of NR–NS structure even decreased a little compared to ZnO NRs. This was due to the decreased electron lifetime of NR–NS structure ZnO as shown in Fig. 5c as calculated from eqn (1), though the R_{ct} increased. The decreased electron lifetime indicated that electrons in the conductive band of ZnO became easier to recombine with the redox in the electrolyte. This could explain the decreased V_{oc} when the NR–NS structure was formed compared to NR. From eqn (2), D_n was also calculated and is shown in Fig. 5d. The results showed lower D_n in NR–NS structured ZnO film as increased R_d as shown in Fig. 5b. As the L_n is directly related to charge transport and charge recombination, the performance of DSCs was investigated to find out how the electron diffusion length (L_n) changed with different morphologies of ZnO. As shown in Fig. 5e, the L_n of NRs structured ZnO was over 60 μm, which was more than the thickness of the film. However, the L_n decreased to about 20 μm when the morphology changed to the NR–NS structure, which was smaller than the thickness of the ZnO film. This results also further indicated charge recombination could be more serious in the NR–NS hierarchical structures. Furthermore, the charge resistance also affects the FF of devices.

Series resistance (R_s) is well known as a key factor that affects the FF. R_s is mainly composed of the resistance of the conductive glass, the resistance of the electron transport within TiO_2 and the bulk resistance of the electrolyte. The following five equations reveal the relationship between FF and R_s.[45] In eqn (4), R_{ch} represents the characteristic resistance of the solar cell. In eqn (5), R_s and r_s represent the series resistance and the normalized series resistance, respectively. In eqn (6), v_{oc} was defined as normalized V_{oc}, k is Boltzman's constant and T is the temperature in Kelvin.[51] In eqn (7), FF_0 was denoted as the idealized fill factor, which could be considered as the same for the two different structures as V_{oc} did not change clearly.

$$R_{ch} \approx V_{oc}/J_{sc} \quad (4)$$

$$R_s \approx R_s/R_{ch} \quad (5)$$

$$v_{oc} = \frac{q}{nkT}V_{oc} \quad (6)$$

$$FF_0 = \frac{v_{oc} - \ln(v_{oc} + 0.72)}{v_{oc} + 1} \quad (7)$$

$$FF = FF_0(1 - r_s) \quad (8)$$

From NR the ZnO to the NR–NS structure, R_s increased as shown in Fig. 5a, which could increase the value of r_s. The increased r_s could decrease FF from eqn (8). However, the value of R_{ch} decreased due to the clearly increased J_{sc}, which was shown in the I–V curve. From eqn (5), this indicated that decreased R_{ch} could increase r_s. From eqn (8), FF decreased from the NR to the NR–NS structure.

As a result, the analysis of EIS could explain the decrease of V_{oc} and FF, which limited the improvement of performance through such attached nanosheets onto the nanorods to form hierarchical structures. Optimization such as decreasing the film thickness could be applied to further improve the performance of devices based on such structures in future study.

To investigate the formation mechanism of NR–NS hierarchically structured ZnO films, detailed time-dependent evolutions of morphology were examined by SEM at different growth stages (2, 4, 6 and 8 h) at 70 °C, which showed the highest conversion efficiency. As shown in Fig. 6a, in the early stage (2 h), a few small sized nanoparticles started to attach on the nanorods. After reaction for 4 h, many thin nanosheets emerged on the nanorods, as shown in Fig. 6b. Fig. 6c was the sample collected at 6 h, showing the presence of NSp whose size was much smaller than that of nanoflowers assembled by NRs. As the reaction proceeded further (8 h), the nanoflower assembly turned to a quite large sized sphere, whose size is almost as same as the nanoflowers composed of NRs. According to the present results and those reported previously,[38,52–54] the evolution process for the assembly of the NS from nanoparticles into NSp is illustrated in Fig. 7. This process started with the formation of large numbers of small-sized nanoparticles capped by citrate. Then, the nanoparticles underwent oriented attachment, inducing formation of NS attached on the NRs, shown as processes (i) and (ii) in Fig. 7. Subsequently, the NS

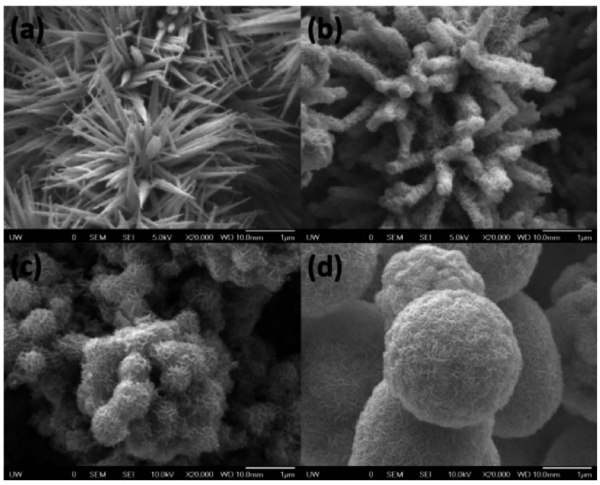

Fig. 6 SEM image of NR–NS hierarchically ZnO on zinc foil obtained by secondary precipitation using $Zn(NO_3)_2$, HMT and sodium citrate, based on the nanorod assembled nanoflowers with different reaction times at 70 °C: (a) 2 h, (b) 4 h, (c) 6 h, (d) 8 h.

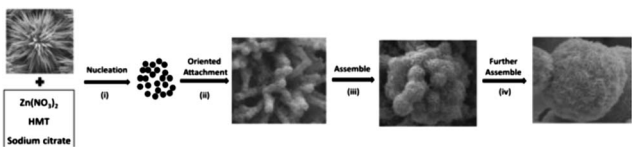

Fig. 7 Schematic illustration of the formation process of ZnO NR–NS hierarchically structured NSp at 70 °C.

assembled at a higher level due to their lateral interactions, and the hierarchical structure was shaped to NSp with relatively smaller size, shown as process (iii) in Fig. 7. Finally, large sized NSp were formed, shown as process (iv) in Fig. 7.[38]

As shown in Fig. 2, different morphologies were formed at different temperature from the second step precipitation based on NRs assembled nanoflowers. At lower temperature (60 °C), NS attached NR structures were formed. As the temperature was increased to 70 °C, the morphology turned to a cauliflower structure composed of submicron sized spheres of 500–700 nm. When the temperature was increased further to 80 °C, the cauliflower structure turned to whole spheres of several micrometers in diameter. To further investigate the mechanism of the formation process, SEM images of ZnO obtained by direct precipitation of $Zn(NO_3)_2$, HMT and sodium citrate without zinc foil at different temperature with 12 h reaction time were tested. As shown in Fig. 8a, NS were obtained at 60 °C, indicating that they could not assemble as NSp even if the reaction time was prolonged to 12 h at such low temperature. The structure obtained at 70 °C is shown in Fig. 8b, indicating that NSp could be assembled as the reaction time was prolonged at such a temperature, as also observed at 80 °C. This result was different from those shown in Fig. 2e and f and in Fig. 6c. Notably, the cauliflower structure which was best for photovoltaic performance, was only obtained at 70 °C and a shorter reaction time such as 6 h. A thermodynamic driving force will ultimately lead

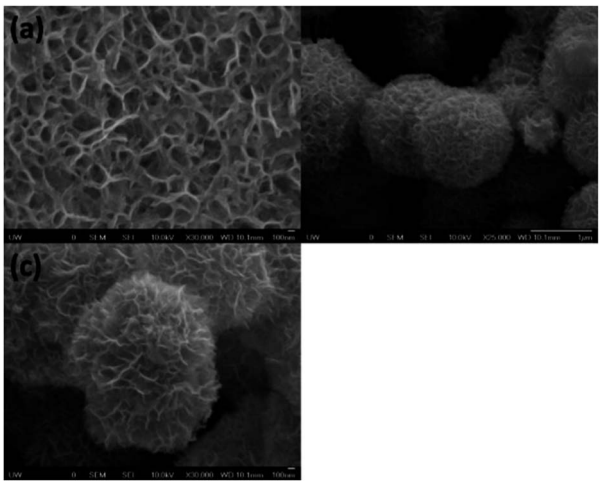

Fig. 8 SEM images of different ZnO morphologies obtained by direct precipitation of $Zn(NO_3)_2$, HMT and sodium citrate without zinc foil in aqueous solution at different temperatures: (a) 60 °C, (b) 70 °C, (c) 80 °C.

to NS assembling as NSp. Fig. 9 shows the temperature–time curve of precipitation using $Zn(NO_3)_2$, HMT and sodium citrate without zinc foil based on the results shown in Fig. 8. This curve could explain the mechanism of formation of different morphologies obtained at different temperatures and reaction times. To assemble NSp composed of NS, a temperature higher than a critical value, which is between 60 and 70 °C was necessary. This is an energy barrier for the assembling of NSp, and also explains the morphologies shown in Fig. 2c and d and Fig. 8a. The processes (i) and (ii) shown in Fig. 7 could occur and the nanosheets will attach on the nanorods. However, the process (iii) could not occur due to the energy barrier. When the temperature is increased to 70 °C, the energy barrier is no longer the main factor affect the morphology, but rather the reaction time. When the reaction time is 6 h a cauliflower structure is formed. However, whole spheres are formed as the reaction time is prolonged to 8 h, as shown in Fig. 6d. As the temperature is further increased to 80 °C, the reaction rate also increased and whole NSp are assembled after a reaction time of 6 h, shorter than that at 70 °C.

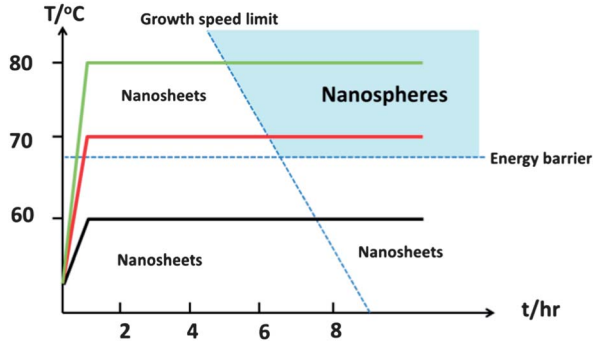

Fig. 9 Temperature–time curve of precipitation results using $Zn(NO_3)_2$, HMT and sodium citrate without zinc foil in aqueous solution.

4 Conclusions

Nanoflowers composed of nanorods (NR) and different nanorod–nanosheet (NR–NS) hierarchical structures were grown on zinc foil and were used as flexible photoanodes for dye-sensitized solar cells. Compared to NR structure, the NR–NS hierarchical structure improved photovoltaic performance of DSCs by increasing the photocurrent significantly. The increased photocurrent was mainly due to larger surface area and dye-loading amount. However, the V_{oc} and FF decreased as the electron transport was more difficult when the 1-D structure was changed to the 3-D structure. Furthermore, the formation mechanism of NR–NS hierarchical structures at different reaction conditions was investigated. This led to optimization of the parameters of such structured ZnO film to obtain higher conversion efficiency. Further study about enhancing conversion efficiency of DSCs based on hierarchical structures is ongoing.

Acknowledgements

This work was supported in part by the US Department of Energy, Office of Basic Energy Sciences, Division of Materials and Engineering under Award no. DE-FG02-07ER46467 (Q. F. Z.) on the microstructure characterization and some power conversion efficiency measurements, National Science Foundation (DMR-1035196), the National Natural Science Foundation of China under Grant no. 50873055 and the National Key Basic Research and Development Program of China under Grant no. 2009CB930602. R. Gao would also like to thank the China Scholarship Council (CSC) for providing a scholarship for PhD study at the University of Washington.

Notes and references

1 B. Oregan and M. Gratzel, *Nature*, 1991, **353**, 737.
2 D. Kuang, C. Klein, S. Ito, J.-E. Moser, R. Humphry-Baker, S. M. Zakeeruddin and M. Graetzel, *Adv. Funct. Mater.*, 2007, **17**, 154.
3 L. Hu, S. Dai, J. Weng, S. Xiao, Y. Sui, Y. Huang, S. Chen, F. Kong, X. Pan, L. Liang and K. Wang, *J. Phys. Chem. B*, 2007, **111**, 358.
4 R. Gao, L. Wang, B. Ma, C. Zhan and Y. Qiu, *Langmuir*, 2010, **26**, 2460.
5 R. Gao, B.-B. Ma, L.-D. Wang, Y.-T. Shi, H.-P. Dong and Y. Qiu, *Acta Phys. Chim. Sin.*, 2011, **27**, 413.
6 R. Gao, L. Wang, Y. Geng, B. Ma, Y. Zhu, H. Dong and Y. Qiu, *Phys. Chem. Chem. Phys.*, 2011, **13**, 10635.
7 R. Gao, L. Wang, Y. Geng, B. Ma, Y. Zhu, H. Dong and Y. Qiu, *J. Phys. Chem. C*, 2011, **115**, 17986.
8 R. Gao, G. Niu, L. Wang, Y. Geng, B. Ma, Y. Zhu, H. Dong and Y. Qiu, *Phys. Chem. Chem. Phys.*, 2012, **14**, 5973.
9 Q. B. Meng, K. Takahashi, X. T. Zhang, I. Sutanto, T. N. Rao, O. Sato, A. Fujishima, H. Watanabe, T. Nakamori and M. Uragami, *Langmuir*, 2003, **19**, 3572.
10 E. Figgemeier and A. Hagfeldt, *Int. J. Photoenergy*, 2004, **6**, 127.
11 P. M. Sommeling, M. Spath, H. J. P. Smit, N. J. Bakker and J. M. Kroon, *J. Photochem. Photobiol., A*, 2004, **164**, 137.
12 S. Nakade, T. Kanzaki, S. Kambe, Y. J. Wada and S. Yanagida, *Langmuir*, 2005, **21**, 11414.
13 M. Gratzel, *C. R. Chim.*, 2006, **9**, 578.
14 A. R. S. Priya, A. Subramania, Y.-S. Jung and K.-J. Kim, *Langmuir*, 2008, **24**, 9816.
15 G. Niu, L. Wang, R. Gao, B. Ma, H. Dong and Y. Qiu, *J. Mater. Chem.*, 2012, **22**, 16914.
16 A. Yella, H. W. Lee, H. N. Tsao, C. Y. Yi and A. K. Chandiran, *Science*, 2011, **334**, 1203.
17 M. Matsumura, S. Matsudaira, H. Tsubomura, M. Takata and H. Yanagida, *Ind. Eng. Chem. Prod. Res. Dev.*, 1980, **19**, 415.
18 G. Redmond, D. Fitzmaurice and M. Graetzel, *Chem. Mater.*, 1994, **6**, 686.
19 H. Rensmo, K. Keis, H. Lindstrom, S. Sodergren, A. Solbrand, A. Hagfeldt, S. E. Lindquist, L. N. Wang and M. Muhammed, *J. Phys. Chem. B*, 1997, **101**, 2598.
20 K. Sayama, H. Sugihara and H. Arakawa, *Chem. Mater.*, 1998, **10**, 3825.
21 K. Keis, E. Magnusson, H. Lindstrom, S. E. Lindquist and A. Hagfeldt, *Sol. Energy Mater. Sol. Cells*, 2002, **73**, 51.
22 T. Stergiopoulos, I. M. Arabatzis, H. Cachet and P. Falaras, *J. Photochem. Photobiol., A*, 2003, **155**, 163.
23 N. G. Park, M. G. Kang, K. S. Ryu, K. M. Kim and S. H. Chang, *J. Photochem. Photobiol., A*, 2004, **161**, 105.
24 S. Ito, N.-L. C. Ha, G. Rothenberger, P. Liska, P. Comte, S. M. Zakeeruddin, P. Pechy, M. K. Nazeeruddin and M. Graetzel, *Chem. Commun.*, 2006, 4004.
25 X. Liu, Y. Luo, H. Li, Y. Fan, Z. Yu, Y. Lin, L. Chen and Q. Meng, *Chem. Commun.*, 2007, 2847.
26 Y.-H. Lai, C.-Y. Lin, H.-W. Chen, J.-G. Chen, C.-W. Kung, R. Vittal and K.-C. Ho, *J. Mater. Chem.*, 2010, **20**, 9379.
27 L.-Y. Lin, M.-H. Yeh, C.-P. Lee, C.-Y. Chou, R. Vittal and K.-C. Ho, *Electrochim. Acta*, 2012, **62**, 341.
28 T. Guo, Y. Chen, L. Liu, Y. Cheng, X. Zhang, Q. Li, M. Wei and B. Ma, *J. Power Sources*, 2012, **201**, 408.
29 X. F. Wu, H. Bai, C. Li, G. W. Lu and G. Q. Shi, *Chem. Commun.*, 2006, 1655.
30 C.-T. Wu, W.-P. Liao and J.-J. Wu, *J. Mater. Chem.*, 2011, **21**, 2871.
31 S. H. Ko, D. Lee, H. W. Kang, K. H. Nam, J. Y. Yeo, S. J. Hong, C. P. Grigoropoulos and H. J. Sung, *Nano Lett.*, 2011, **11**, 666.
32 Y. F. Zhu, G. H. Zhou, H. Y. Ding, A. H. Liu, Y. B. Lin and N. L. Li, *Cryst. Res. Technol.*, 2010, **45**, 1075.
33 S. Yodyingyong, Q. Zhang, K. Park, C. S. Dandeneau, X. Zhou, D. Triampo and G. Cao, *Appl. Phys. Lett.*, 2010, **96**, 073115.
34 W. Zhang, R. Zhu, X. Liu, B. Liu and S. Ramakrishna, *Appl. Phys. Lett.*, 2009, **95**, 043304.
35 J.-Y. Liao, B.-X. Lei, H.-Y. Chen, D.-B. Kuang and C.-Y. Su, *Energy Environ. Sci.*, 2012, **5**, 5750.
36 T. P. Chou, Q. Zhang and G. Cao, *J. Phys. Chem. C*, 2007, **111**, 18804.

37 C. Xu, J. Wu, U. V. Desai and D. Gao, *J. Am. Chem. Soc.*, 2011, **133**, 8122.
38 H. Lu, S. Wang, L. Zhao, J. Li, B. Dong and Z. Xu, *J. Mater. Chem.*, 2011, **21**, 4228.
39 Q. Wang, S. Ito, M. Graetzel, F. Fabregat-Santiago, I. Mora-Sero, J. Bisquert, T. Bessho and H. Imai, *J. Phys. Chem. B*, 2006, **110**, 25210.
40 T. Hoshikawa, R. Kikuchi and K. Eguchi, *J. Electrochem. Soc.*, 2006, **588**, 59.
41 R. Kern, R. Sastrawan, J. Ferber, R. Stangl and J. Luther, *Electrochim. Acta*, 2002, **47**, 4213.
42 J. Bisquert, *J. Phys. Chem. B*, 2002, **106**, 325.
43 Q. Wang, J. E. Moser and M. Gratzel, *J. Phys. Chem. B*, 2005, **109**, 14945.
44 F. Fabregat-Santiago, J. Bisquert, G. Garcia-Belmonte, G. Boschloo and A. Hagfeldt, *Sol. Energy Mater. Sol. Cells*, 2005, **87**, 117.
45 K. Park, Q. Zhang, B. B. Garcia and G. Cao, *J. Phys. Chem. C*, 2011, **115**, 4927.
46 B. C. O'Regan and F. Lenzmann, *J. Phys. Chem. B*, 2004, **108**, 4342.
47 A. Zaban, M. Greenshtein and J. Bisquert, *ChemPhysChem*, 2003, **4**, 859.
48 S. Nakade, Y. Saito, W. Kubo, T. Kitamura, Y. Wada and S. Yanagida, *J. Phys. Chem. B*, 2003, **107**, 8607.
49 L. M. Peter, E. A. Ponomarev and D. J. Fermin, *J. Electrochem. Soc.*, 1997, **427**, 79.
50 J.-Y. Liao, B.-X. Lei, D.-B. Kuang and C.-Y. Su, *Energy Environ. Sci.*, 2011, **4**, 4079.
51 D. Qin, Y. Zhang, S. Huang, Y. Luo, D. Li and Q. Meng, *Electrochim. Acta*, 2011, **56**, 8680.
52 M. Yang, K. Sun and N. A. Kotov, *J. Am. Chem. Soc.*, 2010, **132**, 1860.
53 L. Xu, Y.-S. Ding, C.-H. Chen, L. Zhao, C. Rimkus, R. Joesten and S. L. Suib, *Chem. Mater.*, 2008, **20**, 308.
54 M. Yang, G. Pang, J. Li, L. Jiang, D. Liang and S. Feng, *J. Phys. Chem. C*, 2007, **111**, 17213.